JMEPEG (2017) 26:3901–3914
DOI: 10.1007/s11665-017-2805-5

1059-9495/$19.00

Furnace Brazing Parameters Optimized by Taguchi Method and Corrosion Behavior of Tube-Fin System of Automotive Condensers

J.C. Guía-Tello, M.A. Pech-Canul, E. Trujillo-Vázquez, and M.I. Pech-Canul

(Submitted March 7, 2017; in revised form May 23, 2017; published online June 21, 2017)

Controlled atmosphere brazing has a widespread industrial use in the production of aluminum automotive heat exchangers. Good-quality joints between the components depend on the initial condition of materials as well as on the brazing process parameters. In this work, the Taguchi method was used to optimize the brazing parameters with respect to corrosion performance for tube-fin mini-assemblies of an automotive condenser. The experimental design consisted of five factors (micro-channel tube type, flux type, peak temperature, heating rate and dwell time), with two levels each. The corrosion behavior in acidified sea-water solution pH 2.8 was evaluated through potentiodynamic polarization and electrochemical impedance spectroscopy (EIS) measurements. Scanning electron microscope (SEM) and energy-dispersive x-ray spectroscopy (EDS) were used to analyze the microstructural features in the joint zone. The results showed that the parameters that most significantly affect the corrosion rate are the type of flux and the peak temperature. The optimal conditions were: micro-channel tube with 4.2 g/m^2 of zinc coating, standard flux, 610 °C peak temperature, 5 °C/min heating rate and 4 min dwell time. The corrosion current density value of the confirmation experiment is in excellent agreement with the predicted value. The electrochemical characterization for selected samples gave indication that the brazing conditions had a more significant effect on the kinetics of the hydrogen evolution reaction than on the kinetics of the metal dissolution reaction.

Keywords aluminum, automotive, brazing, corrosion, heat exchanger, Taguchi optimization

1. Introduction

Aluminum heat exchangers have been used extensively in automotive applications such as radiators, heater cores, oil coolers, intercoolers, evaporators and condensers (Ref 1, 2). The condenser of the automotive air-conditioning unit is an aluminum heat exchanger generally manufactured by brazing extruded micro-multiport tubes (in which refrigerant flows) and corrugated fins (which exchange heat with the air side) (Ref 3, 4). Aluminum brazing involves joining the components with a brazing alloy, which is an aluminum-silicon alloy whose melting point is appreciably lower than that of the components; this filler metal is supplied in the fins as a thin clad on both sides of a core alloy. During the brazing process at around 600 °C, the low melting point Al-Si cladding alloy melts and flows, to provide upon cooling a metallic bond between the fins and micro-multiport tubes. The quality of the joints made by brazing depends not only on the proper selection of the filler material, but on many other conditions which need to be kept under control, for instance, a precisely defined temperature range, a rigorously controlled gas atmosphere (high-purity nitrogen, with very low oxygen and water vapor content) and the use of a non-corrosive flux to remove surface oxide films (Ref 5-7). All of these conditions are well specified in a state-of-the-art brazing process under the trade name Nocolok® (Ref 8).

A comprehensive analysis of the joint quality must involve several aspects, such as: (a) appearance, (b) mechanical integrity, (c) microstructure of the joint, and (d) corrosion resistance. The main focus of this work is on the aspect of corrosion resistance. The condenser is normally installed in the neighborhood of the front grill of the automobile, so it is exposed to the environment and consequently suffers external corrosion. Of main concern is the possibility of tube perforation, leading to coolant leaking (Ref 9). Conventionally, the tube is protected by sacrificing the fins, choosing the right alloy composition to reduce its corrosion potential (Ref 10, 11). Another method consists in forming a Zn diffusion layer on the surface of the tube material (Ref 12-15). Zinc has a much lower galvanic potential than aluminum and basically acts as a sacrificial material, so that in the case of an eventual corrosion attack on the micro-channel tube it will spread over the surface rather than create a cavity (i.e., deep pitting is prevented).

The most common accelerated testing to measure the corrosion resistance of heat exchanger materials is the seawater acetic acid test (SWAAT) (Ref 16). It is often used as a quality control and the test criteria are the days till perforation of the material occurs. A SWAAT performance of minimum 20 days is commonly requested by the automotive industry. Although such a test is generally accepted as a good simulation of service life, there are several drawbacks such as its long duration and

J.C. Guía-Tello, E. Trujillo-Vázquez, and **M.I. Pech-Canul**, Cinvestav-Saltillo, Av. Industria Metalúrgica No. 1062 Parque Industrial, 25900 Ramos Arizpe, Coahuila, Mexico; and **M.A. Pech-Canul,** Departamento de Física Aplicada, Cinvestav-Mérida, Km. 6 ant. carr. a Progreso, AP 73 Cordemex, 97310 Mérida, Yucatan, Mexico. Contact e-mail: max@mda.cinvestav.mx.

the low reproducibility. Thus, some authors have used laboratory-based studies under well-controlled conditions to evaluate the corrosion performance of heat exchanger components immersed in SWAAT solution (Ref 11, 17-22). Meijers et al. (Ref 11) showed that using polarization curves as a first screening for materials selection in fin-tube systems can be a powerful tool. Afshar et al. (Ref 17-19) performed a thorough investigation on the relationship between microstructure and electrochemical reactivity for aluminum brazing sheet.

It is very important to consider that the corrosion behavior of the condensers does not depend only on the material selection (e.g., careful selection of alloys for the different components), but also on the metallurgical changes that they experience during the brazing process. Tierce et al. (Ref 23, 24) and Tu et al. (Ref 25) have discussed the changes in microstructure as well as Si-diffusion characteristics for brazing sheets. Furthermore, Laferrere et al. (Ref 20) studied the effect of microstructure on the corrosion behavior of extruded heat exchanger aluminum alloys. Similarly, Klyszewsky et al. (Ref 26) investigated the effect of chemical composition and structure on the corrosion resistance of plated aluminum alloy strips, while Wang and Jiao (Ref 21) reported the microstructural effects in corrosion of aluminum tube alloys. According to Birol et al. (Ref 27) micro-galvanic effects between the intermetallic phases and the aluminum matrix significantly affect the corrosion behavior of aluminum fin stock. As pointed out by Afshar et al. (Ref 17), there are various material-related parameters that can affect the SWAAT performance, including those directly related to the initial condition and others (e.g., brazing temperature and flux load) related to the secondary metallurgical changes during the brazing process.

So, the object of this work is to optimize the process parameters for brazing the tube-fins system of an automotive condenser, in order to achieve excellent corrosion performance together with a good joint size. Optimization was carried out by means of the Taguchi method. This method uses a special design of orthogonal arrays to evaluate the effect of processing variables with a minimum of experiment trials at a relatively low cost (Ref 28). In this work, a standard Taguchi L8 orthogonal array was chosen to analyze the effect of the following factors and interactions: type of micro-channel tube, flux type, peak temperature, dwell time, heating rate, (micro-channel tube) × (peak temperature) and (micro-channel tube) × (dwell time). Analysis of variance of means and analysis of signal-to-noise ratio to 95% confidence level were performed to know the significant factors and interactions on the response variable (corrosion current density).

2. Experimental Procedure

2.1 Materials and Processing

The materials for the tube-fin system were supplied by Airtemp de México as pre-assembled mini-cores, ready for brazing, as shown in Fig. 1(a). The corrugated fins consisted of a brazing sheet (temper: H14) which was 16 mm wide and 80 μm thick; modified AA3003 was used as core material, and it was clad on both surfaces with AA4343 (using a clad ratio of 10% on both sides). Table 1 shows the compositions of core and filler alloys. For the extruded micro-multiport tubes, two candidate aluminum alloys with similar compositions were evaluated (see Table 2), both with H112 temper. In the as-received condition, they had an amount of thermally sprayed Zn which during the brazing process (around 600 °C) diffuses inwards, forming a zinc diffusion layer (the sacrificial layer). The main difference between the two alloys is the amount of sprayed zinc.

The flux was applied to the mini-cores by the dry electrostatic method. Two types of commercial fluxes were evaluated: the standard Nocolok® flux (potassium fluoroaluminate) and an improved formula containing lithium (Nocolok® Li flux) which reduces the solubility of post-braze flux residue (Ref 29).

The controlled atmosphere furnace was a THERMOLYNE 59300 horizontal furnace provided with an alumina tube (92 cm long × 6.9 cm in diameter) sealed at both ends with aluminum caps and with the aid of O-rings. For each test, the mini-core sample was placed in a region of uniform temperature at the center of the alumina tube (the temperature profile in the furnace was previously characterized). Ultra-high-purity nitrogen (UHP 99.999%) was supplied at a constant flow rate of 450 cm^3/min. The dew-point was measured with an Extech psychrometer model RH360.

2.2 Design of Experiments

The five processing parameters were selected, and their corresponding levels are shown in Table 3. Factor A relates to the micro-channel tube, and the two levels correspond mainly to different amounts of sprayed zinc (which as a consequence might result in different concentration profiles of zinc during the brazing process). Factor B corresponds to the type of flux (with or without lithium), which might have an influence on corrosion performance due to the presence of the post-braze flux residue (Ref 8). Factors C, D and E are more directly related to furnace operating parameters (peak temperature, heating rate and dwell time, respectively). The levels for factors C and E were chosen so as to cover a possible range where optimal conditions to obtain a good joint could potentially exist. Concerning factor D, heating rates of 20 °C/min or higher are generally recommended; however, we used lower values in order to maintain a region of uniform temperature at the center of the furnace. The Taguchi L8 orthogonal array is presented in Table 4 and includes the following interactions: A × C (micro-channel tube × peak temperature) and A × E (micro-channel tube × dwell time). The design consists of eight experimental tests which were carried out randomly. For each experiment, three trials were performed to achieve high accuracy in the data. The samples corresponding to the eight experiments were labeled as TA1, TA2, TA3 and so on. The response variable to be optimized is the corrosion current density i_{corr} (μA/cm^2).

In order to determine the percent contribution of factors and the processing parameters that have influence in the mean and the variability on the relevant response, analysis of variance of means (ANOVA) and signal-to-noise ratio analysis (S/N ANOVA) were conducted. The signal-to-noise ratio was computed according to Eq 1,

$$\frac{S}{N} = -10\mathrm{Log}_{10}(\mathrm{MSD}) \qquad \text{(Eq 1)}$$

where MSD is the mean squared deviation. Of the three possible categories of S/N ratios (lower is best, larger is best, or nominal is best), we selected the "nominal is best" criterion for the corrosion current density. The reason for not selecting "lower is best" (corresponding to a minimization of the cor-

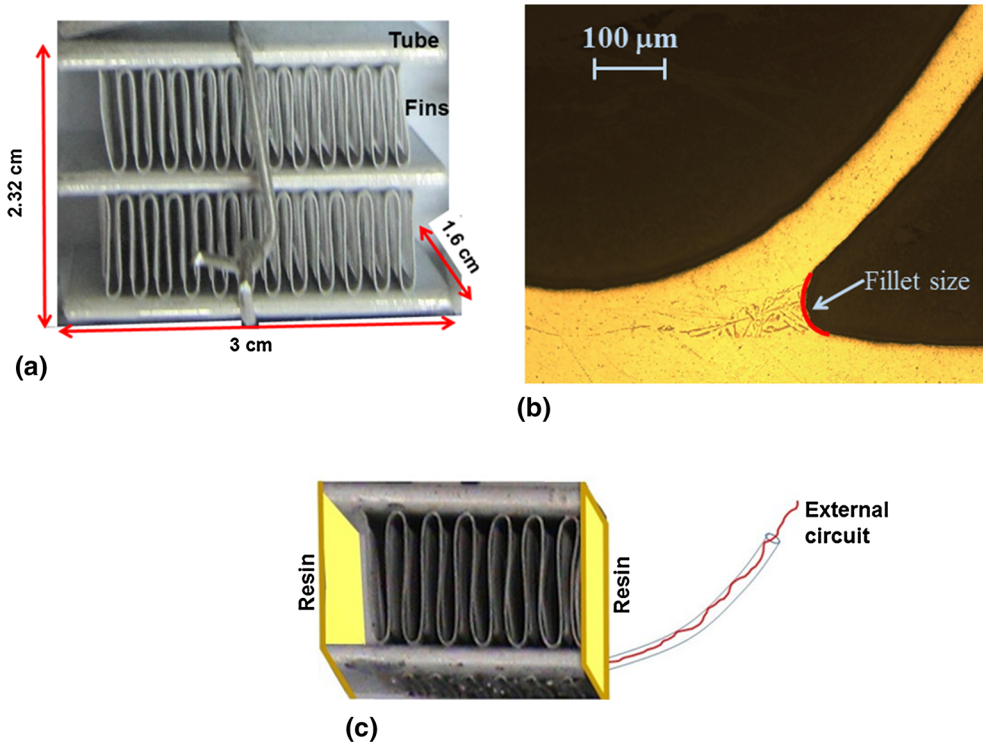

Fig. 1 (a) Condenser mini-core before brazing, (b) tube-fin joint showing with red line the fillet size, (c) tube-fin mini-assembly for electrochemical measurements

Table 1 Compositions (wt.%) of the core and filler alloys in the brazing sheet fin, Temper H14

	Si	Fe	Cu	Mn	Mg	Cr	Zn	Ti	Other	Al
Core										
Max	0.6	0.3	0.05	1.5	0.05	0.12	2.4	0.05	0.15	bal
Min	0.2	…	…	1.0	…	…	2.0	…	…	
Clad										
Max	9.5	0.8	0.4	0.1	0.05	0.05	0.1	0.05	0.15	bal
Min	7.9	…	0.3	…	…	…	…	…	…	

Table 2 Composition of candidate tube alloys, Temper H112

		Composition (wt.%)								
	Zn coating (g/m^2)	Si	Fe	Cu	Mn	Mg	Cr Zn	Ti	other	Al
Tube I	5.5	0.2	0.2	0.4	0.1	0.05	0.05	0.05	0.15	bal
Tube II	4.2	0.14	0.12	0.5	0.17	0.032	0.002	0.02		bal

Table 3 L8 orthogonal array factors and levels

		Levels	
Factor ID	Description	1	2
A	Micro-channel tube	Tube I	Tube II
B	Flux	Standard	With Li
C	Peak temperature, °C	600	610
D	Heating rate, °C/min	5	10
E	Dwell time, min	2	4

Table 4 Experimental layout of Taguchi L8 orthogonal array

	Factors and interactions						
Sample ID	**A**	**A × C**	**C**	**A × E**	**E**	**B**	**D**
TA1	1	1	1	1	1	1	1
TA2	1	1	1	2	2	2	2
TA3	1	2	2	1	1	2	2
TA4	1	2	2	2	2	1	1
TA5	2	1	2	1	2	1	2
TA6	2	1	2	2	1	2	1
TA7	2	2	1	1	2	2	1
TA8	2	2	1	2	1	1	2

rosion rate) is because we observed that a low corrosion rate does not necessarily correspond to a joint with good fillet size. So, our approach was to select as target value of corrosion current density the one that corresponds to the experiment with best fillet size. The MSD was calculated according to,

$$\mathrm{MSD} = \frac{1}{N} * \sum_{i=1}^{N} (Y_i - Y_0)^2 \qquad \text{(Eq 2)}$$

where Y_i and Y_0represent, respective, the observation i and the target value. N denotes the total number of the observations.

Finally, the prediction of the response variable was performed and a confirmation test was carried out in triplicate for the validation of the results.

2.3 Microstructure Characterization

Samples of post-brazed mini-cores were mounted in slow setting Epofix resin, and the cross section was ground with abrasive paper of grit size up to 1200, followed by polishing with Alpha alumina of 1, 0.3 and 0.05 μm. In the final step, the samples were polished with colloidal silica of 0.04 μm. The microstructure at a section of the tube-fin joint was examined for selected samples with a PHILLIPS XL30 ESEM scanning electron microscope coupled with an energy-dispersive x-ray (EDX) detector. Elemental mapping using quantitative x-ray mapping was conducted on the fin and the joint area to identify the nature of main constituent particles.

Zinc concentration profiles in the sacrificial layer of post-brazed micro-channel tube samples were obtained by x-ray energy-dispersive line scans.

Optical images were also acquired with an Olympus VANOX AHMT3 Metallographic microscope with Qimaging MicroPublisher 3.3 RTV camera. The Image Pro-Plus software was used to analyze the images and to perform measurements of fillet size (as shown in Fig. 1b) in triplicate for each sample.

2.4 Electrochemical Characterization

In order to evaluate the overall corrosion behavior of the fins and external surface of the micro-channel tubes (mimicking external corrosion of the condenser under complete wetting conditions), tube-fin mini-assemblies were immersed at ambient temperature in SWAAT solution prepared according to ASTM G85-09 A3 (Ref 16). Two of these mini-assemblies were cut out from each brazed mini-core. A copper wire was attached to the sample for electrical connection, and the ends of the tubes were sealed with epoxy resin to avoid penetration of solution to the micro-channels (Fig. 1c).

The electrochemical measurements were carried out in a three-electrode cell configuration using a Gamry series G300 potentiostat/galvanostat. An Ag/AgCl reference electrode and a counter electrode consisting of a large area Pt foil were used in the cell. The corrosion potential under open circuit conditions (E_{oc}) for each mini-assembly sample was recorded during 1 h, and an electrochemical impedance spectroscopy (EIS) measurement was carried out immediately, using a sine wave perturbation signal with 10 mV amplitude in the frequency range of 10 KHz-250 mHz with five points per decade. Finally, a potentiodynamic polarization curve was obtained at a scan rate of 1 mV/s in the range of ±300 mV versus E_{oc}, starting at a potential 300 mV more negative than E_{oc}.

As indicated above, each trial of the Taguchi design was performed in triplicate. This means that three mini-cores were brazed for TA1, three for TA2 and so on. Since two mini-assemblies like the one shown in Fig. 1(c) were prepared from each mini-core, a total of six repetitions of electrochemical measurement were obtained.

3. Results and Discussion

3.1 Electrochemical Behavior of Tube-Fin Mini-assemblies

In Table 5, the first column shows the sample ID for the eight Taguchi experiments, and columns 2-6 show the corresponding values of each factor. The post-brazed mini-cores for the whole set are expected to exhibit significant differences in electrochemical behavior when immersed in the SWAAT solution; however, it is not the intention to discuss the results of electrochemical measurements for all of them. Only four representative Taguchi experiments were chosen (TA1, TA3, TA4 and TA8). Figure 2 shows typical corrosion potential curves over time for the selected samples. They all exhibit a shift of E_{oc} toward less negative values during the 1-h immersion period. This behavior has been ascribed to dissolution of the oxide film and a gradual consumption of the sacrificial zinc diffusion layer (Ref 30). Furthermore, the four samples have different initial values of E_{oc}. This feature can be related to the fact that the corresponding mini-cores were brazed using different levels for the five factors. For instance, the samples TA1, TA3 and TA4 were brazed using the same type of micro-channel tube (tube I), but due to variations in the other factors they exhibit different initial values of E_{oc} (with a maximum difference of ~42 mV). As the surface of the tube in

each sample changes due to gradual dissolution of the zinc sacrificial layer, E_{oc} evolves to less negative values and, at the end, their corrosion potentials get very close to each other. It is interesting to compare the behavior of samples TA4 and TA1 because they differ only in the peak temperature and dwell time. The sample brazed at the lower temperature and lower dwell time (TA1) exhibits more negative values of corrosion potential during the whole immersion period. A comparison between samples TA1 and TA8 is also useful because they differ only in the type of tube and the heating rate. Sample TA8 was fabricated with tube type II. Its initial value of E_{oc} is very similar to that of sample TA1, but exhibits only a slight shift in potential during the same immersion period. This suggests that the type of micro-channel tube may play an important role in corrosion behavior.

Figure 3 shows the comparison of typical polarization curves for the selected experiments. The corrosion potentials determined from the polarization behavior (indicated by small arrows on the x-axis) follow the same trend observed for E_{oc} in Fig. 2 (e.g., the corrosion potential for sample TA8 is the most negative). An important observation is that, although the corrosion potential values for samples TA1, TA3 and TA4 are very close to each other, their i_{corr} values (determined with a Tafel extrapolation procedure) have quite different values, following the trend $i_{corr}^{TA3} > i_{corr}^{TA4} > i_{corr}^{TA1}$. This can be explained as follows, according to the mixed potential theory: the anodic branches of the three polarization curves have very little separation between them, thus suggesting that they have a nearly constant anodic Tafel slope. On the other hand, the cathodic branches are well separated, with magnitudes of cathodic current density in the order TA3 > TA4 > TA1. This suggests that the differences in i_{corr} (and therefore in corrosion rate) for samples TA1, TA3 and TA4 are mainly due to differences in the kinetics of the cathodic reaction (hydrogen evolution). It appears that these samples have different values of exchange current density (and possibly of cathodic Tafel slopes). As discussed in a previous publication (Ref 30), the electrochemical behavior of the tube-fin system results from the galvanic coupling of the two components. For the combination of materials used in the fabrication of the mini-cores, it can be anticipated that the tube material exhibits anodic behavior (due to sacrificial action of the zinc diffusion layer), while the fins exhibit a cathodic behavior. Variations in the furnace parameters during the brazing process (heating rate, peak temperature and dwell time) are expected to yield different zinc concentration profiles in the tube (and therefore a different concentration of zinc at the surface). It appears that for the samples TA1, TA3 and TA4 such changes in the surface condition did not significantly affect the kinetics of the anodic reaction. On the other hand, the fins are made from a brazing sheet. So, the variations in furnace parameters are clearly expected to produce significant metallurgical changes in the fins. Since the surface in contact with the electrolyte is the residual clad, the differences in its microstructure are more likely responsible for differences in the kinetics of the hydrogen evolution reaction for samples TA1, TA3 and TA4. In Ref 30, it was shown that when the Zn-coated tube and the fins are uncoupled, the tube has a more negative corrosion potential (and also a lower i_{corr}) compared to the fins. According to the mixed potential theory for bimetallic systems, the tube-fin mini-assembly adopts a common potential in between the corrosion potential of individual elements. It is evident in Fig. 3 that sample TA8 exhibits a lower i_{corr} compared to the other three samples. This can be explained assuming that for this system i_{corr} decreases because the corrosion potential of the couple gets very close to the uncoupled potential of the tube.

The results of EIS measurements obtained for samples TA1, TA3, TA4 and TA8 after 1-h immersion in the SWAAT solution are presented as Nyquist plots in Fig. 4. Each diagram exhibits the typical impedance response for aluminum in acidic chloride solutions (Ref 31-34), which consists of a capacitive loop at

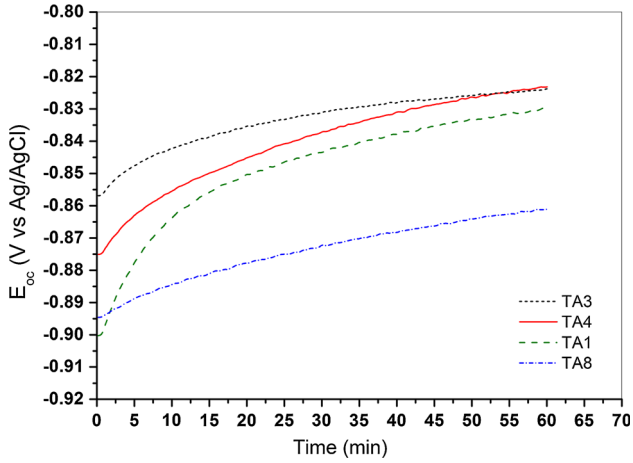

Fig. 2 Variation of the open circuit potential as a function of time for selected samples (TA1, TA3, TA4 and TA8) immersed in SWAAT solution

Table 5 Experimental design, response and *S/N* ratio

	Factors					Corrosion current density, μA/cm^2				
Sample ID	A	B	C	D	E	R_1	R_2	R_3	Avg.	$(S/N)_{NB}$, dB
TA1	Tube I	Standard	600	5	2	50.51	29.54	49.40	43.15	−34.76
TA2	Tube I	With Li	600	10	4	172.64	87.31	141.40	133.78	−34.14
TA3	Tube I	With Li	610	10	2	218.19	126.29	225.54	190.01	−40.29
TA4	Tube I	Standard	610	5	4	84.49	152.18	54.51	97.06	−32.22
TA5	Tube II	Standard	610	10	4	139.46	107.43	158.73	135.21	−32.80
TA6	Tube II	With Li	610	5	2	116.64	116.02	156.23	129.63	−31.52
TA7	Tube II	With Li	600	5	4	133.83	137.01	66.81	112.55	−31.10
TA8	Tube II	Standard	600	10	2	38.87	26.63	31.11	32.20	−36.26

$(S/N)_{NB}$: signal-to-noise ratio. Nominal is the best
R_1, R_2 and R_3 are the replicas of experimental design

high frequencies (HF) followed by an inductive loop in the low frequency(LF) range. The HF capacitive loop can be correlated to the dielectric properties of the oxide film, present even in acidic solutions (Ref 33). For the inductive loop, various interpretations have been given in the literature. In this work, it was attributed to the coverage relaxation of the adsorbed intermediate H_{ads} in the reduction of H^+ (Ref 30, 34, 35). The equivalent circuit most commonly used to fit the experimental impedance data is shown in Fig. 5(a). R_s is the solution resistance, Q and α are parameters associated with a constant phase element (CPE), R_p is the polarization resistance, L and R_{ind} are the elements related to the inductive loop. As shown in the schematic diagram in Fig. 5(b), the charge transfer resistance R_{ct} is obtained from the addition of R_p and R_{ind}. The CPE is usually introduced to account for non-ideal capacitive behavior of the interfacial charge storage mechanism. The non-ideal behavior is related to a frequency dispersion phenomenon which may have different origins (Ref 36, 37); in this case, it can be attributed to roughness and possibly a non-uniform potential and current distribution associated with electrode geometry. The admittance for this circuit element is given by $Y_{CPE} = Q(j\omega)^{\alpha}$, where ω is the sine wave modulation angular frequency, Q is the CPE coefficient (with dimensions Ω^{-1} s^{α} cm^{-2}), and α is an empirical exponent ($0 \leq \alpha \leq 1$) which measures the deviation from the ideal capacitive behavior. A sufficiently good fit of the experimental impedance data in Fig. 4 with the equivalent circuit in Fig. 5(a) was obtained (see comparison of experimental and fitted data in the Bode plots in Fig. 6). The optimum fit parameters are presented in Table 6. A column with the values of the effective interfacial capacitance (C_{eff}) calculated from the fit parameters related to the HF loop is included. They were calculated with the following relationship for a surface time-constant distribution (Ref 37):

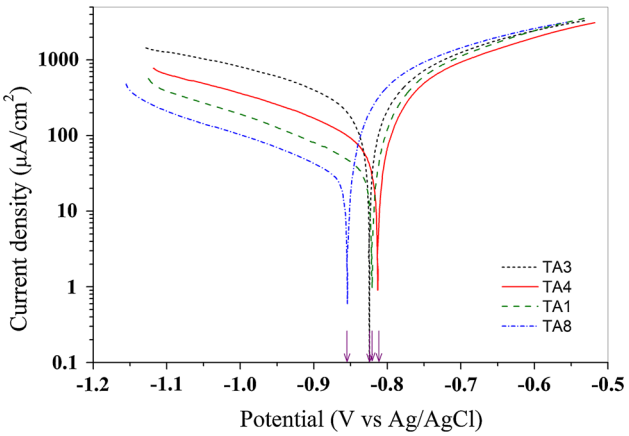

Fig. 3 Typical polarization curves for selected samples (TA1, TA3, TA4 and TA8), obtained after 1-h immersion in SWAAT solution. Scan rate = 1 mV/s

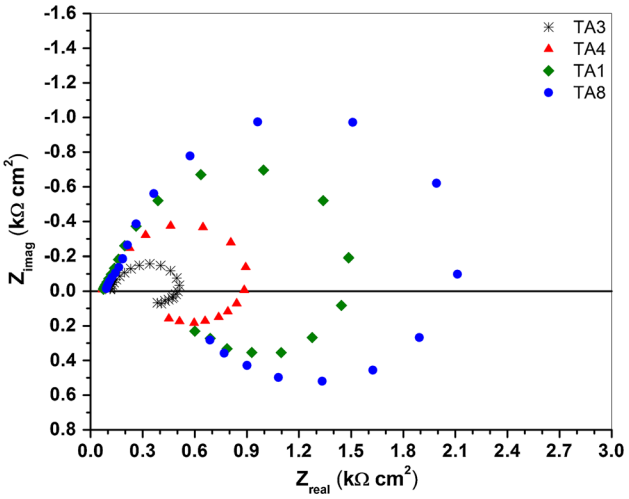

Fig. 4 Nyquist diagrams obtained for selected samples (TA1, TA3, TA4 and TA8) after 1-h immersion in SWAAT solution

$$C_{eff} = Q^{1/\alpha}\left(\frac{R_s R_p}{R_s + R_p}\right)^{(1-\alpha)/\alpha} \quad \text{(Eq 3)}$$

It can be observed that these values are lower than the typical value of the double layer capacitance C_{dl} (50 μF cm^{-2}). This means that the HF interfacial capacitance represents a series connection between C_{dl} and the oxide film capacitance C_{ox} $\left(\frac{1}{C_{eff}} = \frac{1}{C_{dl}} + \frac{1}{C_{ox}}\right)$. The estimated values of C_{ox}, assuming C_{dl} = 50 μF cm^{-2}, are around 3 μF cm^{-2}, in good agreement with reported values of this capacitance for a thin barrier oxide film on aluminum (Ref 38, 39). In Table 6, a column for the charge transfer resistance ($R_{ct} = R_p + R_{ind}$) is also included. According to the Stern-Geary equation, i_{corr} is proportional to the reciprocal of R_{ct} $\left(i_{corr} = B/R_{ct}\right)$. The

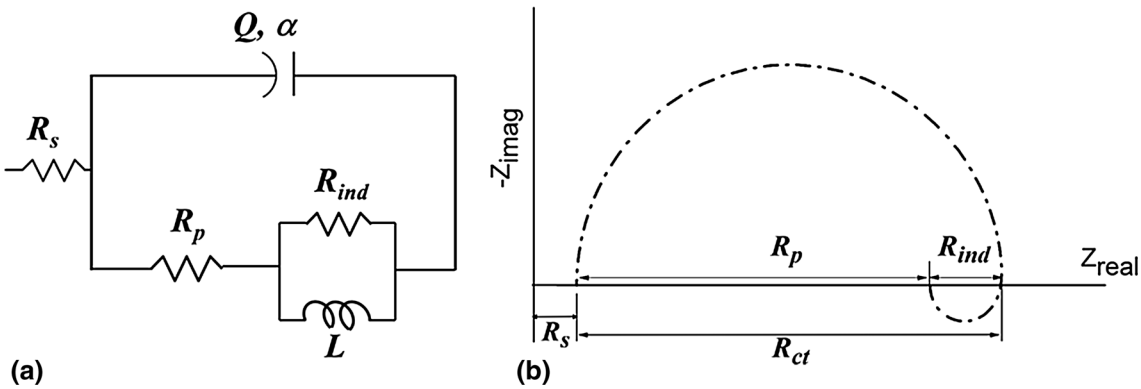

Fig. 5 (a) Equivalent circuit model used to analyze the experimental data in Fig. 4, (b) schematic Nyquist diagram corresponding to the circuit in (a)

proportionality constant B depends on the anodic and cathodic Tafel slopes. Assuming that B is roughly constant for the four samples, the increasing values of R_{ct} in Table 6 would correspond to decreasing values of i_{corr}. This trend is in good agreement with the results obtained with the polarization curves: $i_{corr}^{TA3} > i_{corr}^{TA4} > i_{corr}^{TA1} > i_{corr}^{TA8}$.

3.2 Distributions of Corrosion Current Density and Fillet Size

As indicated above, the response variable to be optimized is i_{corr}. This can be calculated by two methods: by Tafel extrapolation using the polarization curves or from the Stern-Geary equation using the R_{ct} values determined from EIS measurements. As shown in the previous section, both methods give consistent results. So, for the statistical analysis it was decided to use the values calculated from polarization curves. Average values of i_{corr} and S/N ratios for all the Taguchi experiments are presented in Table 5 (columns 7-11). The maximum average value is 190 μA/cm^2 for TA3, and the minimum is 32.2 μA/cm^2 for TA8. Additionally, the data are presented as a bar diagram in Fig. 7(a). The variability in values of the corrosion current density gives evidence that there is clearly an influence of brazing parameters on the corrosion performance.

In principle, the optimization procedure would be oriented to the minimization of i_{corr} to ensure a low corrosion rate of the automotive condenser in the SWAAT solution. However, the results in this study show that there is another aspect of joint quality that needs to be taken into account: the joint size. Figure 7(b) shows the distribution of fillet sizes that were obtained for the brazed mini-cores. It is clear that the lowest corrosion current density value (that for TA8) does not correspond to the best fillet size (in fact it corresponds to the smallest). Based on this observation, it was decided to perform the optimization under the criterion of "nominal is best," choosing as target value of corrosion current density the one that corresponds to the experiment with best fillet size (TA4). This is indicated schematically with an arrow in Fig. 7.

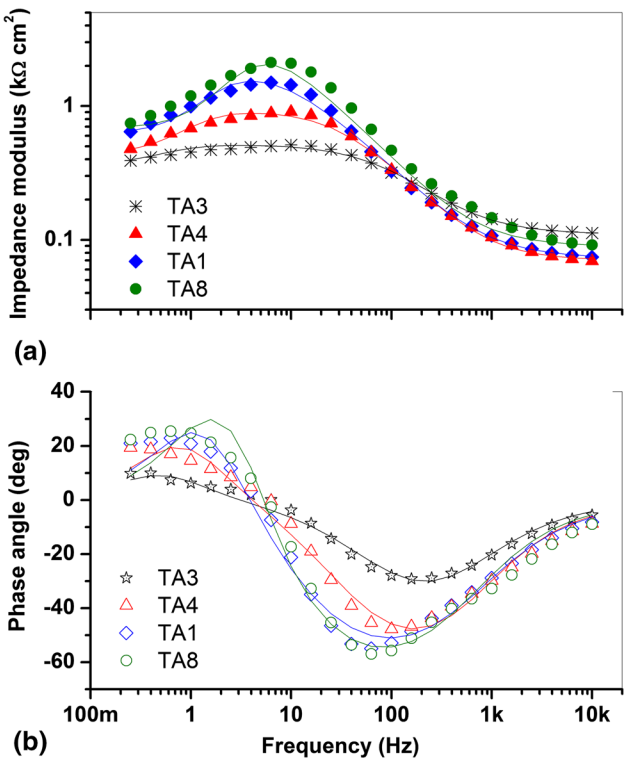

Fig. 6 Bode plots comparing experimental impedance data (symbols) and fitted data (lines) for the selected samples (TA1, TA3, TA4 and TA8). (a) Modulus, (b) phase angle

3.3 Microstructural Characterization

Figure 8 shows typical SEM micrographs of the tube-fin joints corresponding to post-brazed mini-cores TA4 and TA1. Figure 8(a), corresponding to sample TA4, resembles a typical very good fin-to-tube joint (Ref 6, 40). The joint for sample TA1 (Fig. 8b) exhibits a lower quality. According to Table 5, the only difference between these two samples is in the thermal treatment. TA4 was brazed at 610 °C during 4 min, while TA1 was brazed at 600 °C during 2 min. Apart from the evident effect on fillet length, this is expected to yield different microstructural features which in consequence affect the corrosion performance. The results of i_{corr} in Table 5 actually show that the corrosion rate of TA4 is about twice that of TA1. So, it is interesting to analyze the microstructural features around the joint for these two samples. In Fig. 9(a), a SEM backscattered electron image of the fillet in sample TA4 is presented. The characteristic Al-Si network with Si present as a needle-like structure is clearly observed, along with some block-like precipitates appearing in bright contrast (like the one circled in red). A similar type of particle was observed by Lacaze et. al. (Ref 23, 24) in the joint zone of two brazed multilayer sheets (modified AA3003 core, clad on both faces with AA4343) and was identified as the Al-Fe-Mn-Si phase. In this work, the results of EDS mapping of alloying elements Fe, Mn and Si (Fig. 9c, d and e) suggest that these precipitates correspond rather to the Al-Mn-Fe phase. Silicon is present only in the needle-like structure. Figure 10(a) shows the SEM backscattered electron image of a small section of the fins in the joint zone of the same sample TA4. Several elongated bright particles (like the ones circled in red) can be observed. It has been extensively discussed in the literature (Ref 18-20, 41, 42) that during brazing Si diffuses from the melted cladding to the core material leading to the transformation of $Al_6(Mn, Fe)$ precipitates to phases containing Al, Mn, Fe and Si. The results of EDS mapping of the main alloying elements (Fig. 10c, d and

Table 6 Parameters from equivalent circuit analysis of impedance spectra in Fig. 4

Sample	R_s, Ω cm^2	$Q \times 10^5$, Ω^{-1} cm^{-2} s^{α}	α	C_{eff}, μF cm^{-2}	R_p, Ω cm^2	R_{ind}, Ω cm^2	L, H cm^2	R_{ct}, Ω cm^2
TA3	109.9	1.66	0.80	3.1	260.4	151.6	40.0	412.0
TA4	69.6	1.26	0.83	2.9	373.2	494.7	66.8	867.9
TA1	72.2	1.83	0.79	3.0	554.3	1212.0	85.9	1766.3
TA8	88.6	1.30	0.82	2.9	600.0	1900.0	75.0	2500.0

e) confirm that these particles correspond to the Al-Fe-Mn-Si phase. It has been proposed that the presence of these particles helps in corrosion protection of the core (Ref 41).

As described earlier, the anodic reaction takes place mainly on the micro-channel tube, while the cathodic reaction takes place mainly on the fins. The results of electrochemical measurements showed that the difference in corrosion rate between samples TA4 and TA1 is mainly due to variations in the kinetics of the hydrogen evolution reaction. So, it is interesting to compare the microstructure in the fins for these two samples. Figure 11(a) shows the SEM backscattered electron image of a small section of the fins in the joint zone of sample TA1. Again, some bright particles corresponding to the Al-Fe-Mn-Si phase can be observed (confirmed by the EDS mappings in Fig. 11c, d and e). The Si map in Fig. 11(e) shows the presence of large silicon particles in the re-solidified clad. Apparently not enough diffusion of Si occurred from the melted cladding to the core material due to the lower temperature and dwell time of sample TA1 (as compared to sample TA4). Some of the Al_6(Mn, Fe) precipitates in the core that did not transform to AlFeMnSi are shown in Fig. 11(c). These results give an indication that the fins in samples TA4 and TA1 have different Si concentrations at the surface (higher in the case of sample TA1), and this may be the reason for the variations in the kinetics of the hydrogen evolution reaction.

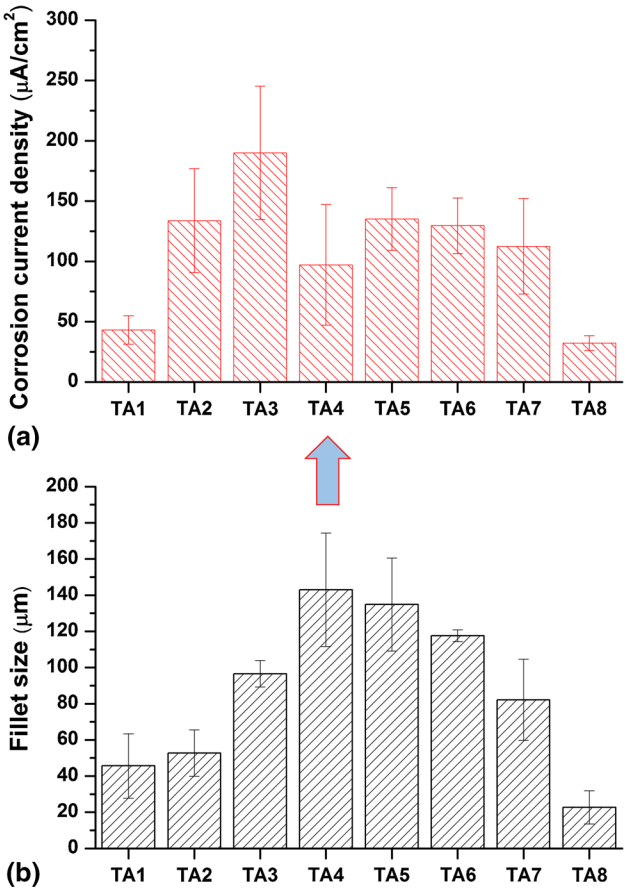

Fig. 7 Bar diagrams for: (a) corrosion current density and (b) fillet size

In the case of the micro-channel tubes, the difference in thermal treatment for samples TA4 and TA1 is expected to affect the diffusion of zinc during the brazing process. Figure 12 shows a comparison of Zn concentration profiles obtained with EDS line profile analysis, starting from the external surface. It is evident that for depths below the surface of 5-60 μm, the Zn concentration is higher in sample TA1. Due to higher temperature and dwell time for sample TA4, the amount of zinc near the surface decreased because it penetrated more into the tube material (e.g., at a depth of 140μm, the concentration is higher for sample TA4). The greater Zn concentration near the surface for sample TA1 explains the more negative values of corrosion potential shown in Fig. 2. Apparently, this difference in surface concentration of Zn in the tubes of samples TA4 and TA1 did not have any significant influence on the kinetics of the anodic reaction (as discussed with the analysis of polarization curves).

The results presented in this section provide evidence that the modifications in microstructure can be correlated to the electrochemical behavior of Taguchi samples TA4 and TA1. A detailed discussion of this correlation for all the other samples is beyond the scope of this work.

3.4 Statistical Analysis

The analysis of effects for means and *S/N* ratio for the corrosion current density is presented in Table 7. It includes ranks based on delta statistics, which compare the relative magnitude of effects. The delta statistics are the highest minus the lowest average for each factor (or interaction). The ranks indicate the relative importance of each factor (or interaction) to

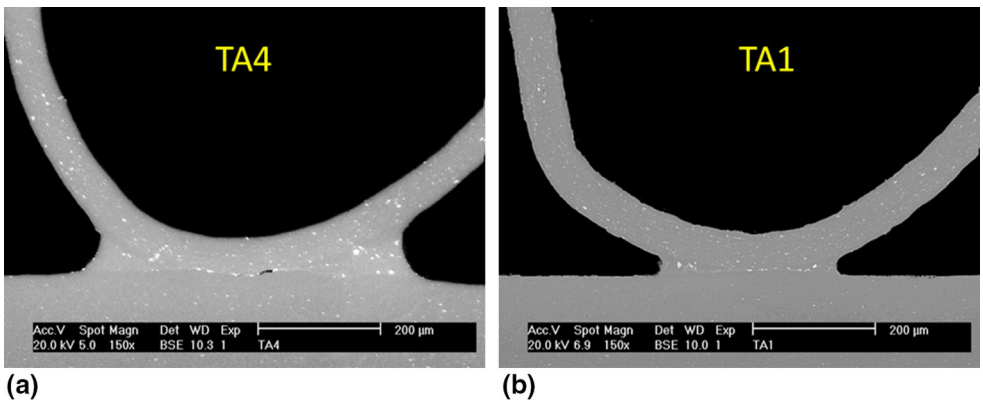

Fig. 8 SEM micrographs of typical tube-fin joints: (a) for sample TA4, (b) for sample TA1

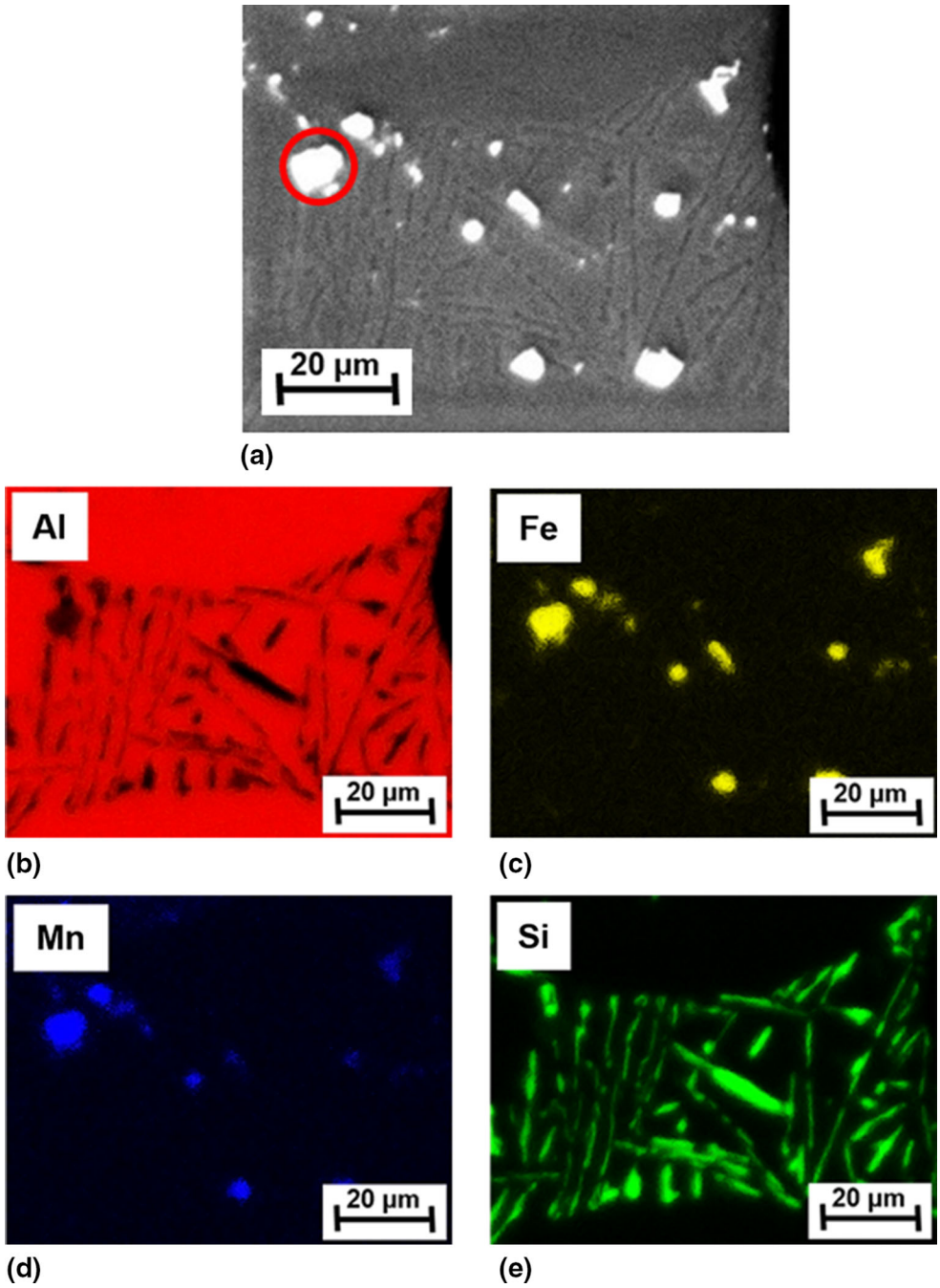

Fig. 9 (a) SEM image for a region in the brazed joint of sample TA4. EDS mapping of: (b) Al, (c) Fe, (d) Mn and (e) Si

the response (rank 1 corresponds to the highest delta values, rank 2 to the second highest, and so on). It is clear that the factors with major effects for the i_{corr} means were (in decreasing order): B (the type of flux), C (the peak temperature) and D (the heating rate). On the other hand, the analysis for *S*/*N* ratio effect suggests that the higher effects on the variability correspond (in decreasing order) to factors D (heating rate), E (dwell time) and A (the type of micro-channel tube).

In order to determine the statistical significance of factors (or interactions) on the mean and the variability in the response variable, an analysis of variance was carried out. The ANOVA of means and *S*/*N* ratio for corrosion current density is presented in Table 8. Both analyses were performed at 95% confidence level. The F_{table} for ANOVA of means was $F_{(0.05,\ 1,1)} = 161.45$ and for ANOVA *S*/*N* ratio was $F_{(0.05,\ 1,2)} = 18.513$. If $F > F_{table}$, the factor is significant at the confidence level used. The results of ANOVA of means show that the most significant factors were B (type of flux) and C (peak temperature). These factors had the highest percentage of contribution on the mean, with values of 44 and 35%, respectively.

The ANOVA of *S*/*N* ratio shows that at the established confidence level, the most significant factors were D (heating rate), E (dwell time), A (micro-channel tube), A × C (micro-channel tube × peak temperature) and A × E (micro-channel tube × dwell time). Their percentage contributions were: 37, 31, 18, 8 and 4%, respectively. The interactions had the lowest contributions to the variability in the current density response,

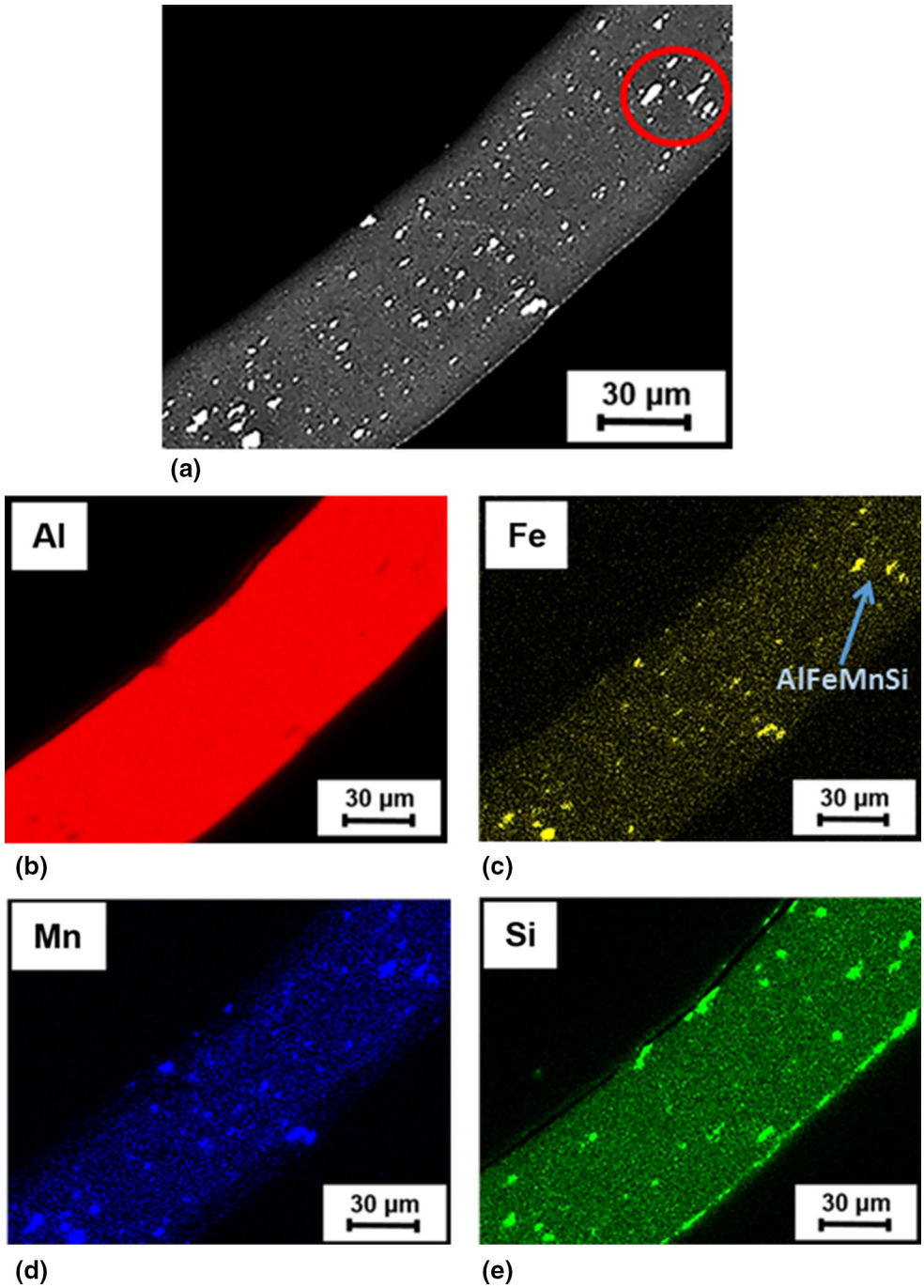

Fig. 10 (a) SEM image for a section of the fin in sample TA4. EDS mapping of: (b) Al, (c) Fe, (d) Mn and (e) Si

so it can be considered that highest contributions are mainly from factors A, D and E. The experimental error of both ANOVAs was 2%.

The factors and levels that adjust the mean to the target value and maximize the *S*/*N* ratio for the response variable (i_{corr}) were chosen taking into account the description of factors/levels in Table 4 and the results of Tables 7 and 8. Accordingly, the factors and levels selected to adjust the mean to the target value were B1 (standard flux) and C2 (610 °C, peak temperature). The factors and levels with the highest *S*/*N* ratio that decrease the variability were A2 (micro-channel tube II), D1 (5 °C/min heating rate) and E2 (4 min dwell time). Therefore, the conditions A2B1C2D1E2 were the most suitable for obtaining the optimal response of i_{corr}.

3.5 Optimal Conditions

The prediction of corrosion current density (nominal is the best) is computed using the optimal conditions A2B1C2D1E2 and significant interactions $A \times C$ and $A \times E$. Since the response i_{corr} involves a target value, the predicted optimal performance ($Y'_{i_{corr}}$) is given by the following equation (Ref 28):

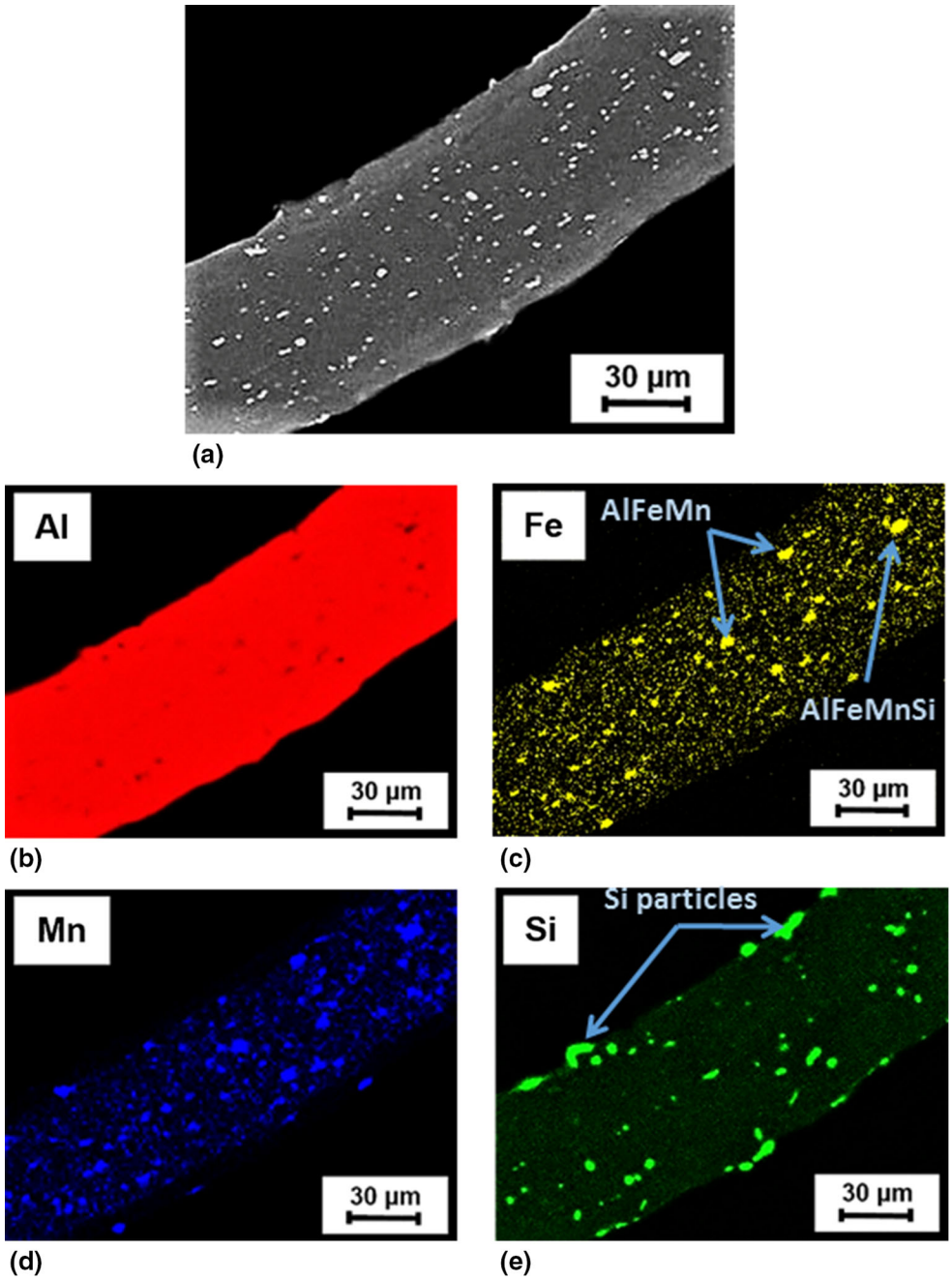

Fig. 11 (a) SEM image for a section of the fin in sample TA1. EDS mapping of: (b) Al, (c) Fe, (d) Mn and (e) Si

$$Y'_{i_{\text{corr}}} = \sqrt{Y_{i_{\text{corr}}}} + Y_{\text{target value}} \quad \text{(Eq 4)}$$

with $Y_{\text{target value}}$ = the fixed value of corrosion current density (97 μA/cm^2. $Y_{i_{\text{corr}}}$ is the mean square deviation (MSD) from the target value, which is computed with the following equation

$$Y_{i_{\text{corr}}} = \bar{Y} + (\bar{A}2 - \bar{Y}) + (\bar{B}1 - \bar{Y}) + (\bar{C}2 - \bar{Y}) + (\bar{D}1 - \bar{Y}) + (\bar{E}2 - \bar{Y}) + (\overline{A2C2} - \bar{Y}) + (\overline{A2E2} - \bar{Y}) \quad \text{(Eq 5)}$$

where $\bar{Y}$ is the grand average of the *S*/*N* ratios of the current density and $\bar{A}2$, $\bar{B}1$, $\bar{C}2$, $\bar{D}1$, $\bar{E}2$, $\overline{A2C2}$ and $\overline{A2E2}$ are the average effects of the *S*/*N* ratios with parameters at their respective optimum levels (Table 7). The result ($Y_{i_{\text{corr}}} = -29.79 \pm 1.24$ Db) was converted back to the units of the original observations: 30.87±4.44 μA/cm^2. Thus, the predicted response is $Y'_{i_{\text{corr}}} = 97 \pm 30.87$ μA/cm^2.

3.6 Verification Tests

Figure 13 shows the representative polarization curve of the confirmation test results evaluated under optimum conditions A2B1C2D1E2 (micro-channel tube type II, standard flux, 610 °C peak temperature, 5 °C/min heating rate and 4 min dwell time). The average of results for three samples obtained

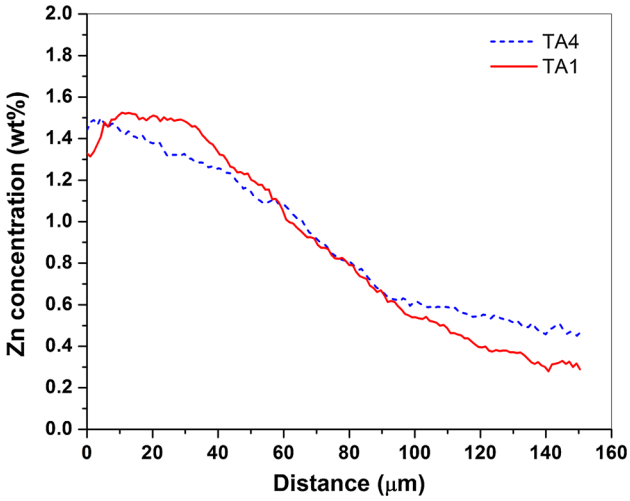

Fig. 12 Zn concentration profiles for micro-channel tubes of samples TA4 and TA1

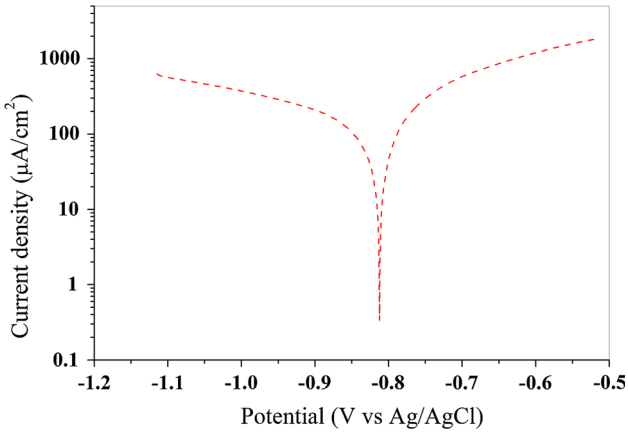

Fig. 13 Typical polarization curve for the confirmation test

Table 7 Response table for mean and *S/N* ratio

		Factors and interactions						
Analysis	**Level**	**A**	**B**	**C**	**D**	**E**	**A × C**	**A × E**
Mean	1	116.00	76.91	80.42	95.60	98.75	110.44	120.23
	2	102.40	141.49	137.98	122.80	119.65	107.96	98.17
	Delta	13.60	64.59	57.55	27.20	20.90	2.49	22.06
	Rank	6	1	2	3	4	7	5
S/N ratio	1	−35.35	−34.01	−34.07	−32.40	−35.71	−33.31	−34.74
	2	−32.92	−34.26	−34.21	−35.87	−32.57	−34.97	−33.54
	Delta	2.43	0.25	0.14	3.47	3.14	1.66	1.20
	Rank	3	6	7	1	2	4	5

Table 8 Results of ANOVA for mean and S/N ratio of corrosion current density

ANOVA	Source of variation	DOF	SS	V	F	S′	P
	A: micro-channel tube	1	370.08	370.082	29.91	357.71	2
	B: type of flux	1	8342.73	8342.73	674.24*	8330.35	44
	C: peak temperature	1	6625.00	6625.00	533.42*	6612.62	35
Mean	D: heating rate	1	1479.84	1479.84	119.60	1467.47	8
	E: dwell time	1	873.75	873.751	70.61	861.38	4
	A × E	1	973.34	973.343	78.66	960.97	5
	Error	1	12.37	12.374			2
	Total	7	18,677.11				
	A: micro-channel tube	1	11.84	11.84	141.04*	11.754	18
	D: heating rate	1	24.11	24.11	287.24*	24.025	37
S/N ratio	E: dwell time	1	19.69	19.69	234.61*	19.607	31
	A × C	1	5.53	5.53	65.85*	5.443	8
	A × E	1	2.90	2.90	34.55*	2.816	4
	Error	2	0.17	0.08			2
	Total	7	64.23				

DOF: degrees of freedom, SS: sum of squares, V: variance, F: variance ratio (* statistically significant at 95% confidence), S′: pure sum of squares, and P: percentage of contribution

by Tafel analysis is 102.07 ± 6.68 μA/cm^2 and agrees very well with the predicted value. Moreover, in Fig. 14 an optical micrograph of this sample in the as-brazed condition (not corroded) is presented. It shows a typical well-brazed tube-fin joint with a joint size (147.84 ± 9.22 μm) in excellent agreement with the selected target value.

4. Conclusions

A Taguchi orthogonal array was employed to optimize the brazing parameters with respect to corrosion performance of tube-fin mini-assemblies in SWAAT solution.

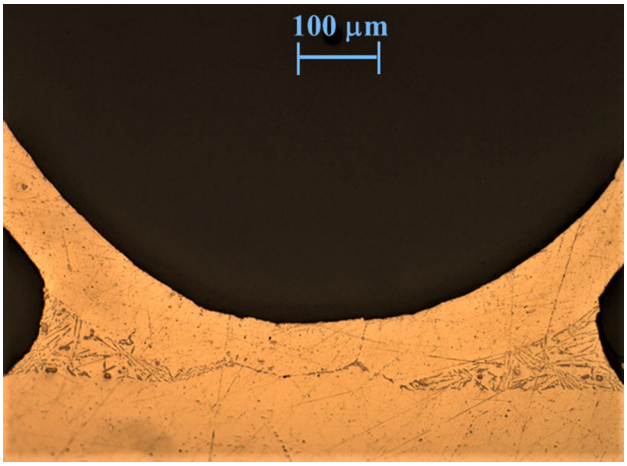

Fig. 14 Optical micrograph of tube-fin joint corresponding to confirmation test

- It was shown that the brazing conditions had an effect not only in the response variable to be optimized (i_{corr}), but also on the fillet size. Thus, the nominal is the best criterion for the *S*/*N* ratio was selected, choosing as target value of i_{corr} that corresponding to the experiment with the maximum fillet size.
- The parameters that most significantly affect the corrosion rate are the type of flux (44%) and the peak temperature (35%). The optimal conditions to adjust the i_{corr} to the target value were: micro-channel tube type II, standard flux, 610 °C peak temperature, 5 °C/min heating rate and 4 min dwell time. The i_{corr} value of the confirmatory experiment is in excellent agreement with the predicted value.
- The results of electrochemical measurements for selected samples immersed during 1 h in SWAAT solution showed that variations in i_{corr} are mainly due to changes in the kinetics of the cathodic reaction.
- The microstructural features in the joint zone for two samples brazed under two different peak temperatures and dwell times were analyzed and correlated with their electrochemical behavior. Variation in kinetics of the hydrogen evolution reaction on the fins was attributed to a different surface concentration of silicon.

Acknowledgments

J.C. Guía-Tello wishes to express his gratitude to Conacyt (National Council of Science and Technology in Mexico) for the scholarship provided for his doctoral studies. The authors are deeply grateful to the Engineering Department of Airtemp de México, S.A. de C.V., for useful feedback and for providing the samples of tube-fin mini-assemblies used in this research. The authors are also grateful to Felipe de Jesús Márquez Torres M.Sc., Dr. Martha Elena Rivas Aguilar and Dr. Miguel Ángel Aguilar González for valuable support with SEM/EDAX analysis, and to Marbella Echeverría for technical assistance with corrosion tests.

References

1. J. Hirsch, Recent Development in Aluminum for Automotive Applications, *Trans. Nonferrous Met. Soc. China*, 2014, **24**, p 1995–2002
2. European Aluminum Association, *AAM-Applications-Power Train-Heat Exchangers,* http://european-aluminium.eu/resource-hub/aluminium-automotive-manual/. Accessed 4 March 2017
3. R.K. Shah and D.P. Sekulić, *Fundamentals of Heat Exchanger Design*, John Wiley & Sons Inc., Hoboken, 2003
4. T. Koppan, *Heat Exchanger Design Handbook*, Marcel Dekker Inc., New York, 2000
5. R. Mundt and H. Koblenz, Introduction to Brazing of Aluminum Alloys, *TALAT Lecture 4601*, European Aluminum Association, 1994
6. R.K. Shah, Advances in Science and Technology of Compact Heat Exchangers, *Heat Transf. Eng.*, 2006, **27**, p 3–22
7. H. Zhao and R. Woods, Controlled Atmosphere Brazing of Aluminum, *Advances in Brazing, Science, Technology and Applications*, D.P. Sekulić, Ed., Woodhead Publishing Ltd., Sawston, 2013,
8. H.W. Swidersky, Aluminum Brazing with Non-Corrosive Fluxes, State of the Art and Trends in Nocolok Flux Technology, *Proc. 6th Int. Conf. on Brazing, High Temperature Brazing and Diffusion Bonding*, Aachen Germany, May 2001
9. M. Melander and R. Woods, Corrosion Study of Brazed Aluminum Radiators Retrieved from Cars After Field Service, *Corrosion*, 2010, **66**, p 0150051–01500514
10. R.D. Tait, C.J. Rogers, A.J. Cottone, J.P. Henkes, and Z.P. Saperstein, Corrosion Resistance of the as Brazed PF Heat Exchanger as Achieved by Alloy Selection, *SAE Technical Paper 910594*, Society of Automotive Engineers, 1991
11. S.D. Meijers, C.E. Calcedo Martinez, and S. Desikan, Tube-Fin Interaction—A Closer Look at the Corrosion Mechanism, *SAE Technical Paper 2005-01-2027*, Society of Automotive Engineers, 2005
12. K. Ishikawa, H. Kawase, H. Koyama, Y. Hasegawa, K. Negura, and M. Nonogaki, Development of Pitting Corrosion Resistant Condenser with Zinc-arc-spray Extruded Multi-Cavity Tubing, *SAE Technical Paper 910592*, Society of Automotive Engineers, 1991
13. Q. Shi, F. Liang, and B. Cheadle, Electrochemical Behaviors of Quad-layer Aluminum Brazing Sheet Composite for Automotive Application, *Corrosion*, 2004, **60**, p 492–500
14. S. Yoon, H. Kim, and Ch Lee, Fabrication of Automotive Heat Exchanger Using Kinetic Spraying Process, *Surf. Coat. Technol.*, 2007, **201**, p 9524–9532
15. G. Parundekar and A. Chavan, Corrosion Life Improvement of All Aluminum Micro Channel Heat Exchangers (MCHX) in HVAC&R Industry, Paper CSD-01, *Int. Corros. Conf. and Expo CORCON2015*, NACE International Gateway India Section, 2015
16. ASTM G85-09, *Standard Practice for Modified Salt Spray (fog) Testing*, ASTM International, 2009
17. F.N. Afshar, E. Szala, A. Witterbrood, R. Mulder, J.M.C. Mol, H. Terryn, and J.H.W. de Wit, Influence of Material Related Parameters in Sea Water Acidified Accelerated Test, Reliability Analysis and Electrochemical Evaluation of the Test for Aluminum Brazing Sheet, *Corros. Sci.*, 2011, **53**, p 3923–3933
18. F.N. Afshar, J.H.W. de Wit, H. Terryn, and J.M.C. Mol, The effect of Brazing Process on Microstructure Evolution and Corrosion Performance of a Modified AA4XXX/AA3XXX Brazing Sheet, *Corros. Sci.*, 2012, **58**, p 242–250
19. F.N. Afshar, F.D. Tichelaar, A.M. Glenn, P. Taheri, M. Sababi, H. Terryn, and J.M.C. Mol, Improved Corrosion Resistance of Aluminum Brazing Sheet by a Post-Brazing Heat Treatment, *Corrosion*, 2017, **73**, p 379–393
20. S. Meijers, *Corrosion of Aluminum Brazing Sheet*, Ph.D. Thesis, Delf University of Technology, 2002
21. A. Laferrere, N. Parson, X. Zhou, and G. Thompson, Effect of Microstructure on the Corrosion Behavior of Extruded Heat Exchanger Alloys, *Surf. Interface Anal.*, 2013, **45**, p 1597–1603
22. G. Wang and H.S. Jiao, Microstructural Effects in Corrosion of Aluminum Tube Alloys, *Trans. Nonferrous Met. Soc. China*, 2011, **21**, p 1193–1198
23. J. Lacaze, S. Tierce, M.-C. Lafont, Y. Thebault, G. Mankowski, C. Blanc, H. Robidou, D. Vaumousse, N. Pébère, and D. Daloz, Study of the Microstructure Resulting from Brazed Aluminum Materials used in Heat Exchangers, *Mater. Sci. Eng. A*, 2005, **413–414**, p 317–321
24. S. Tierce, N. Pébère, C. Blanc, G. Mankowski, H. Robidou, D. Vaumousse, and J. Lacaze, Solidification and Phase Transformations in Brazed Aluminum Alloys used in Automotive Heat Exchangers, *Int. J. Cast Met. Res.*, 2005, **18**, p 370–376

25. Y. Tu, Z. Tong, and J. Jiang, Effect of Microstructure on Diffusional Solidification of 4343/3005/4343 Multi-layer Aluminum Brazing Sheet, *Metall. Mater. Trans. A*, 2013, **44A**, p 1760–1766
26. A. Klyszewski, J. Zelechowski, M. Opyrchal, M. Nowak, A. Frontczak, and P. Rutecki, The effect of Chemical Composition and Structure on the Corrosion Resistance of Plated Aluminum Alloy Strips, *Proc. 13th Int. Conf. on Aluminum Alloys*, The Minerals, Metals & Materials Society, 2012, p 451–457
27. F.S. Birol, Y. Birol, and M. Smalova, Corrosion Behavior of Aluminum Finstock Alloys, *Mater. Sci. Forum*, 2002, **396–402**, p 1511–1516
28. R.K. Ranjit, *A Primer on the Taguchi Method*, Society of Manufacturing Engineers, 210
29. P. García Juan, H.W. Swidersky, T. Schwarze, and J. Eicher, Inorganic Fluoride Materials from Solvay Fluor and Their Industrial Applications, *Chapter 7 in Functionalized Inorganic Fluorides: Synthesis, Characterization & Properties of Nanostructured Solids*, A. Tressaud, Ed., John Wiley & Sons Ltd., Hoboken, 2010, p 205–228
30. M.A. Pech-Canul, J.C. Guía-Tello, M.I. Pech-Canul, J.C. Aguilar, J.A. Gorocica-Díaz, R. Arana-Guillén, and J. Puch-Bleis, Electrochemical Behavior of Tube-Fin Assembly for and Aluminum Automotive Condenser with Improved Corrosion Resistance, *Results Phys.*, 2017, **7**, p 1760–1777
31. C.M.A. Brett, The Application of Electrochemical Impedance Techniques to Aluminum Corrosion in Acidic Chloride Solutions, *J. Appl. Electrochem.*, 1990, **20**, p 1000–1003
32. L. Garrigues, N. Pebere, and F. Dabosi, An Investigation of the Corrosion Inhibition of Pure Aluminum in Neutral and Acidic Chloride Solutions, *Electrochim. Acta*, 1996, **41**, p 1209–1215
33. M. Metikoš-Huković and R. Babić, Impedance Spectroscopic Study of Aluminum and Al-Alloys in Acid Solution: Inhibitory Action of Nitrogen Containing Compounds, *J. Appl. Electrochem.*, 1994, **24**, p 772–778
34. M. Metikoš-Huković, R. Babić, and Z. Grubač, The Study of Aluminum Corrosion in Acidic Solution with Nontoxic Inhibitors, *J. Appl. Electrochem.*, 2002, **32**, p 35–41
35. H.J.W. Lenderink, M.V.D. Linden, and J.H.W. de Wit, Corrosion of Aluminum in Acidic and Neutral Solutions, *Electrochim. Acta*, 1993, **38**, p 1989–1992
36. J.B. Jorcin, M.E. Orazem, N. Pébère, and B. Tribollet, CPE Analysis by Local Electrochemical Impedance Spectroscopy, *Electrochim. Acta*, 2006, **51**, p 1473–1479
37. P. Córdoba-Torres, T.J. Mesquita, O. Devos, B. Tribollet, V. Roche, and R.P. Nogueira, On the Intrinsic Coupling Between Constant-Phase Element Parameters α and Q in Electrochemical Impedance Spectroscopy, *Electrochim. Acta*, 2012, **72**, p 172–178
38. S.E. Frers, M. Stefenel, C. Mayer, and T. Chierchie, AC-Impedance Measurements on Aluminum in Choride Containing Solutions and Below the Pitting Potential, *J. Appl. Electrochem*, 1990, **20**, p 996–999
39. J. Bessone, D.R. Salinas, C.E. Mayer, M. Ebert, and W.J. Lorenz, An EIS Study of Aluminum Barrier-Type Oxide Films in Different Media, *Electrochim. Acta*, 1992, **37**, p 2283–2290
40. H. Zhao, A.J. Salazar, and D.P. Sekulic, Analysis of Fin-Tube Joints in Compact Heat Exchangers, *Heat Transf. Eng.*, 2009, **30**, p 931–940
41. G.J. Marshall, R.K. Bolingbroke, and A. Gray, Microstructural Control in an Aluminum Core Alloy for Brazing Sheet Applications, *Metall. Trans. A.*, 1993, **24A**, p 1935–1942
42. K. Schäuble, *Silica Passivation Layer on Aluminum Brazing Sheets*, Doctoral dissertation, University of Köln, 2010